# A Highly Efficient Microwave Plasma Jet Based on Evanescent-Mode Cavity Resonator Technology

Abbas Semnani, *Senior Member, IEEE*, and Kazi Sadman Kabir

***Abstract*— This article introduces a novel low-power and highly efficient atmospheric pressure microwave plasma jet (APPJ). Specifically, a capillary tube passing through the critical gap area of a high-$Q$ evanescent-mode (EVA) cavity resonator provides a controlled gas flow rate to realize microwave gas breakdown and plasma jet formation even with milliwatts range input power. The theory, simulation, fabrication, and characterization of the introduced plasma jet technology are discussed. A prototype 2.45 GHz device can operate at powers as low as 400 mW with >80% power efficiency and provides up to a 6-mm-long plasma jet with electron density in the range of $10^{15}$ cm$^{-3}$ in a 1 to 7 slpm helium flow rate. Considering its high plasma density as well as low operating power and jet temperature, this device is a viable and safe solution for a wide range of applications, including emerging plasma medicine needs.**

***Index Terms*— Atmospheric pressure, cavity resonator, evanescent mode (EVA), highly efficient, plasma jet.**

## I. Introduction

COLD plasma is a critical technology in many application fields. However, generating stable plasma is not a trivial task as energy-hungry machines are often required. Currently, igniting and sustaining plasma are usually performed by using either high-voltage pulses (e.g., 100 s of V to kV) or high-power radio frequency (RF) sources (e.g., 10 s of W). Therefore, even though low-power plasma with effective surface power density in the order of 0.1–1 W/cm$^2$ is sufficient for many applications, including some medical ones [1], [2], [3], most of the current plasma sources are bulky and expensive units as they are inefficient in transferring energy to the plasma. Hence, efficient plasma with low power consumption is expected to impact a wide range of applications such as plasma medicine, food and water decontamination, lighting, and reconfigurable RF electronics.

Although dc, pulse, and RF plasmas have been extensively explored, there is no comprehensive understanding of microwave plasma. This is despite microwave plasma occurring in the $\alpha$–discharge regime with an extremely low sheath voltage drop, ensuring that the ignited plasma is stable with no electrode erosion as an important lifetime issue [4], [5], [6], [7]. Also, higher degrees of ionization and dissociation, higher density of electrons and reactive species, lower heavy particle temperatures, and lower breakdown voltage are other advantages of microwave plasma compared to other types of electrically excited plasma. Nonresonant microwave plasma sources, however, are also realized by employing bulky and high-power supplies. In addition, they come at a prohibitively high cost except for high-end applications [8]. Moreover, the resulting high voltages reduce power efficiency, require cumbersome safety protocols, and create a poor environment from an electromagnetic (EM) compatibility perspective.

Due to their ability to store and enhance EM energy, it is possible to employ microwave resonant structures to achieve high-efficiency plasma with low power consumption [9], [12], [13], [14]. The main principle is to utilize resonators that can concentrate the EM fields over a small gap. Then, even with considerably low input power levels, the magnitude of EM fields over those critical gaps can reach the breakdown threshold, resulting in gas breakdown and plasma formation. Since the effective size of the gap decreases after plasma formation, the required amount of power for sustaining plasma is usually even less. Before plasma ignition, the unloaded resonator produces strong fields necessary for gas breakdown. The higher the resonator's quality factor, the higher the field enhancement. After ignition, however, the plasma impedance interacts with the resonator, quenching the resonator's quality factor. Thus, resonant structures also operate as so-called "ballast" to avoid plasma instability, such as the glow-to-arc transition and streamer formation [9]. Pulsing the microwave plasma can further decrease power consumption [10], [11].

Different microwave resonant structures (e.g., quarter/half wavelength [13], ring [9], and dielectric [14]) implemented using various technologies (microstrip, stripline, coplanar waveguide, coaxial, etc.) have been successfully examined for low-power plasma creation. However: 1) most of them do not operate in atmospheric pressure, which makes them difficult to be implemented in many practical scenarios; 2) the ignited plasma region is typically confined to a minimal volume and, hence, not optimal for many applications; and 3) it is impractical in most of the cases to scale up the resonant designs to larger areas.

Several atmospheric pressure microwave plasma jets (APPJs) have also been introduced. For example, Srivastava and Wang [15] presented an APPJ in 2011 with helium gas flow rates from 0.38 to 0.78 slpm and under plasma power of 38–78 W at 2.45 GHz, a 2.5–3 mm plasma jet was achieved. Kim *et al.* [16] introduced a microstrip-based microwave-excited APPJ capable of generating a 10-mm wide argon jet at 2.45 GHz, with 20–60 W of input power and 0.3–3.01 lpm flow rate. A couple of years later, Kwon *et al.* [17] presented a coaxial transmission line resonator (CTLR) based

Manuscript received 21 March 2022; revised 6 August 2022; accepted 23 August 2022. Date of publication 9 September 2022; date of current version 21 October 2022. This work was supported in part by the National Science Foundation under Grant ECCS-2102100 and in part by the UToledo College of Engineering Faculty Startup Fund under Grant FSF-110876. The review of this article was arranged by Senior Editor J. G. Leopold. *(Corresponding author: Abbas Semnani.)*

The authors are with the Department of Electrical Engineering and Computer Science, The University of Toledo, Toledo, OH 43606 USA (e-mail: abbas.semnani@utoledo.edu; kazisadman.kabir@rockets.utoledo.edu).

Color versions of one or more figures in this article are available at https://doi.org/10.1109/TPS.2022.3202509.

Digital Object Identifier 10.1109/TPS.2022.3202509

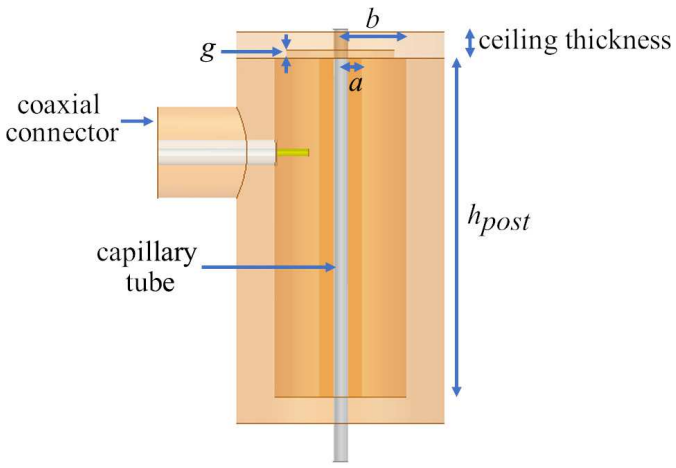


Fig. 1. Structure and main parameters of an EVA cavity resonator-based microwave plasma jet.

Ar plasma operated in the frequency range of 2.3–2.5 GHz with a gas flow rate of 1.5 lpm. This device had a 32.7% maximum power efficiency and 93%, 89%, and 88% power transfer efficiency at forwarding power of 1, 1.5, and 2 W, respectively. Fu *et al.* [18] introduced a coaxial transmission line based microwave excited atmospheric pressure plasma jet (CTL-MAPPJ) operated at 2.45 GHz with two channels of gas input, having Ar gas flow rates of 2 and 1.5 lpm through those gas input channels. With a minimum input power of 31.6 dBm, their device could generate a plasma jet of 3-mm length with 89.6% maximum efficiency.

This article introduces a novel, highly efficient microwave plasma jet based on evanescent-mode (EVA) cavity resonator technology. An EVA cavity resonator is formed by loading a normal cavity by a post at the center. One important consequence of this loading is the electric field concentration in the gap between the resonator post and the top wall. This feature was previously used to implement novel plasma-based high-power microwave limiters and switches [6], [19]. However, this work implements a gas flow mechanism to pass through the EVA critical region to realize a high-efficiency resonant microwave plasma jet. The theory of operation, design process, and modeling results are presented in Section II. Then, in Section III, the fabrication process, experimental setup, and measurement results are discussed. Plasma jet diagnostics are covered in Section IV, followed by a brief conclusion in Section V.

## II. Design and Simulation

An EVA cavity resonator is formed by loading an enclosed cavity with a post in the center [20], [21]. Due to this loading, the electric field gets concentrated in the region between the post and the resonator ceiling, resulting in an effective capacitance. As a result, the size of an EVA cavity resonator reduces significantly compared to an ordinary cavity resonator. The quality factor of EVA cavity resonators is typically high ($\geq$500), which makes them good candidates for many applications, specifically for tunable and selective filters.

Fig. 1 describes the main parameters associated with an EVA cavity resonator. Here, $h_{\text{post}}$, $g$, $a$, and $b$ represent the height of the post, capacitive gap, the radius of the post, and radius of the cavity, respectively. The inductance and capacitance values associated with the structure are crucial to the resonant frequency-the gap results in the capacitance of $C_{\text{gap}}$. The post contributes to the inductance of the cavity, $L_{\text{post}}$, and coaxial capacitance, $C_{\text{coax}}$. Also, $C_{\text{fringe}}$ corresponds to the fringe field effect at the edge of the post

$$L_{\text{post}} = \frac{376.7343}{6\pi \times 10^8} \times \ln\frac{b}{a} \times h_{\text{post}} \tag{1}$$

$$C_{\text{coax}} = \frac{2\pi e_0}{\ln\frac{b}{a}} \times h_{\text{post}} \tag{2}$$

$$C_{\text{gap}} = k_{\text{gap}} \times \frac{\pi e_0 a^2}{g} \tag{3}$$

$$C_{\text{fringe}} = e_0 a \times \ln\left(\frac{a}{2g}\right). \tag{4}$$

Here, $k_{\text{gap}}$ is a coefficient used to adjust the $C_{\text{gap}}$ due to a capillary tube in the gap in the structure introduced in this work. The resonant frequency of the structure can then be represented as

$$f_{\text{res}} = \frac{1}{2\pi\sqrt{L_{\text{post}} C_{\text{total}}}} \tag{5}$$

where $C_{\text{total}}$ is the sum of the above three capacitors, as they are formed in a parallel configuration. The formulas are in accordance with the empirical ones stated in [22].

An EVA cavity resonator is ideal for plasma jet creation because of the structural symmetry and the gas flow that can be conducted through the central post. In the proposed structure, this has been accomplished by drilling a hole through the post. Then a capillary tube was utilized to pass the gas to the outlet through the critical gap area of the EVA resonator. In this case, the capacitive gap is partially filled by the dielectric of the tube. The capillary tube extends up to the external edge of the ceiling to prevent the gas from leaking inside the resonator structure. Because of the hole in the electrode and the presence of the capillary tube, the $C_{\text{gap}}$ is affected, which is incorporated by the $k_{\text{gap}}$ coefficient in (3). With enough input power to the resonator and consequently high electric ($E$) field over the critical gap area of the EVA resonator, the gas going through this area ignites, and the plasma plume gets out because of the gas flow. In this work, a 2.45 GHz resonant frequency was chosen as it is one of the standard frequencies for microwave plasma generation, making it easier to benchmark the proposed EVA cavity plasma jet. However, this technique can be extended to other frequencies.

To address the goal of achieving a highly efficient plasma jet, a very high |E|-field in the critical gap area, between the surface above the post and the ceiling, is of utmost importance. To attain this, a very high $Q$ along with a good matching performance at the resonant frequency of 2.45 GHz are critical. Coming up with the post radius, a capillary tube with 1.12 mm of external diameter should go through the post. To drill a hole to pass this tube, a minimum post radius is necessary. For cavity radius, an optimum $b/a$ of around 3.59 for maximum $Q$ has been reported in the literature [23]. As gas breakdown takes place in the capacitive gap region, the gap size ($g$) has to be such that: 1) there can be enough volume of gas and 2) it is practical regarding the CNC fabrication accuracy. The 50-Ω impedance matching is mainly adjusted by positioning (height) and pin length of the coaxial connector. The connector

TABLE I
PARAMETERS OF THE DESIGNED 2.45 GHz EVA PLASMA JET

| Parameter | Symbol | Dimension (mm) |
|---|---|---|
| cavity radius | $b$ | 5 |
| post radius | $a$ | 1.6 |
| gap | $g$ | 0.6 |
| post height | $h_{post}$ | 25.84 |
| capillary tube inner radius | $r_{tube}$ | 0.45 |
| capillary tube wall thickness | $t_{tube}$ | 0.1 |
| cavity ceiling thickness | $t_{ceiling}$ | 2 |

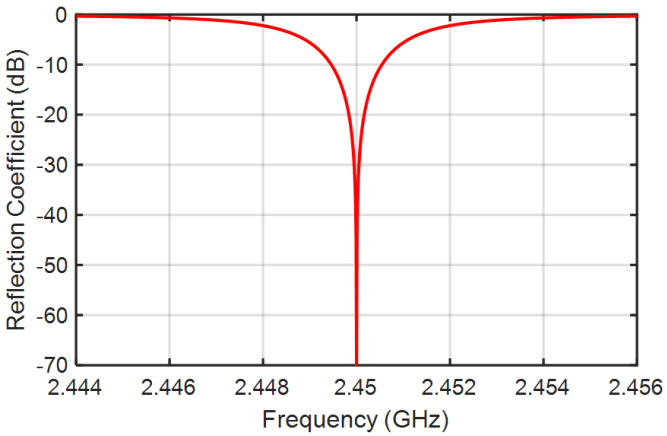


Fig. 2. Simulated reflection coefficient ($S_{11}$) of the designed EVA cavity resonator showing a solid resonance at 2.45 GHz.

pin length must also be adequately long to provide a strong coupling of the input energy to the resonator—a high external coupling coefficient. The dimensions of the designed EVA plasma jet at 2.45 GHz are presented in Table I. The proposed microwave plasma jet operates at atmospheric pressure with a controlled gas flow rate system.

The designed EVA cavity-based plasma jet was simulated using ANSYS HFSS. As seen in Fig. 2, a strong resonance at 2.45 GHz with excellent matching performance was observed. The eigenmode simulated $Q$ of the resonator was calculated to be around 1500, which aligns well with the design requirements. Fig. 3 shows how the $E$-field concentrates in the capillary tube section that passes through the critical gap area over the resonator post. As seen, at the resonant frequency, the device generates an $E$-field in the order of $5.2 \times 10^5$ (V/m) in the critical gap region in the presence of 1 W input power. This strong $E$-field is responsible for the gas breakdown and plasma ignition in that gap.

## III. FABRICATION AND MEASUREMENTS

### A. Fabrication Process

The designed EVA cavity structure was fabricated by copper CNC machining, as seen in Fig. 4. The 0.6 mm critical gap over the post was practically realized by drilling out the gap in the ceiling, as depicted in Fig. 4(a). Since the resonant frequency strongly depends on this gap size, because of its dominant role in $C_{\text{gap}}$, eight screws and a thick wall were considered. Any air gap between the ceiling and the body of the resonator not only affects the resonant frequency but also

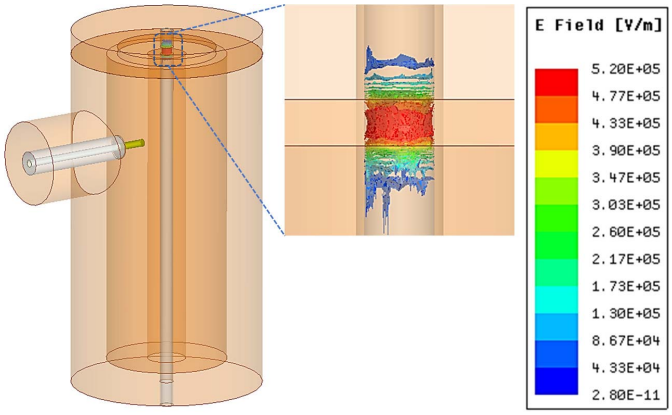


Fig. 3. High concentration of $E$-field in the critical gap area of the designed EVA cavity resonator with 1 W input power at the resonant frequency of 2.45 GHz.

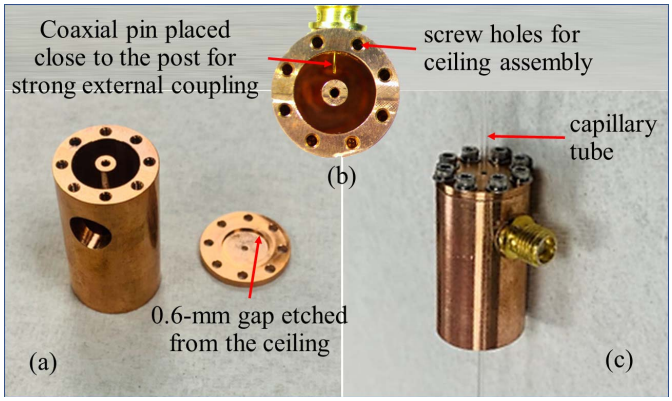


Fig. 4. Fabricated 2.45 GHz EVA cavity plasma jet (a) two parts (body and lid) of the EVA cavity resonator after copper CNC machining, (b) assembly of the push-fit SMA coaxial connector showing that the pin gets close (for strong external coupling) but does not touch the post, and (c) fully assembled EVA cavity plasma jet including a capillary tube to pass the gas flow through the resonator critical gap region. It must be noted that in practice, the capillary tube extends up to the top edge of the resonator ceiling. It was extended more in this image to highlight its placement position.

results in degradation of the resonator $Q$, or equivalently a higher loss.

A push-fit SMA connector was used for easier assembly, as seen in Fig. 4(b). The connector height and pin length are two major parameters regarding impedance matching, optimized in the simulation process. It is noted that the connector pin must get close to the cavity post to generate a strong external coupling of EM energy to the resonator, which is essential for efficient plasma generation. However, it does not touch the post. Through EM simulations seeking a good matching and a strong $E$-field in the resonator gap area, the optimum placement of the SMA connector was found to be at 18.65 mm from the cavity bottom surface, and the optimum distance of the pin of the SMA connector from the post was found to be 0.89 mm. The resonator wall thickness was chosen so that this gap between the coaxial pin and the center post is automatically achieved without trimming the pin length. After the ceiling assembly, a capillary tube is inserted through the post and the ceiling holes. It is made sure that the capillary tube reaches the outlet and barely crosses the surface, enough for the plasma jet to get out. Fig. 4(c) represents the prototype EVA cavity plasma jet after assembly.

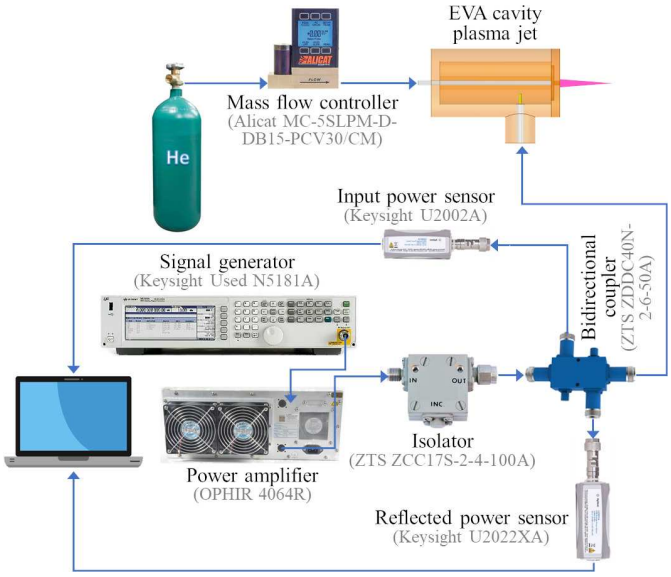


Fig. 5. Block diagram of the EVA cavity microwave plasma jet generation and measurement setup.

### B. Measurement Setup

As presented in Fig. 5, a complete test setup was designed and implemented to accurately characterize the introduced EVA cavity microwave plasma jet. Helium gas was fed to the capillary tube through a mass flow controller (MFC) that can provide an accurate flow rate of up to 7 slpm. A flexible dielectric tube was utilized to connect the MFC and the capillary glass tube. A 2.45 GHz microwave signal generated by a signal generator was fed to the resonator after being amplified by a power amplifier. An isolator is implemented at the output of the amplifier to absorb the reflected power following plasma ignition, as the frequency response of the resonator changes post breakdown. Also, two USB power sensors were used through a high-power bidirectional coupler at the isolator's output for accurate measurement of the forward and reflected powers at the port of the fabricated EVA plasma jet device.

### C. Experimental Results

In the first step, the reflection coefficient of the assembled device was tested to check the resonance behavior. Although this is an OFF-mode test, it must be conducted in the presence of the capillary tube as it affects the $C_{\text{gap}}$ and hence the resonant frequency. As seen in Fig. 6, there is a good match between the simulated and measured $S_{11}$. A 1.1 MHz downward shift in the measured resonant frequency is due to the fabrication and assembly tolerances. Also, as expected, lower $Q$ (higher loss) was observed in measurement- the simulated and measured reflection coefficients are $-70$ and $-18.6$ dB, respectively. This is mainly attributed to the leakage of EM energy from tiny gaps between the resonator body and the ceiling, which is a common practical issue with this structure. Since the measured resonant frequency was 2.4489 GHz, all other measurements were also conducted at this frequency, although it will be referred to as 2.45 GHz in the rest of the text for easier recall.

Fig. 7 shows a sample image of an atmospheric pressure air plasma jet generated by the fabricated EVA cavity structure.

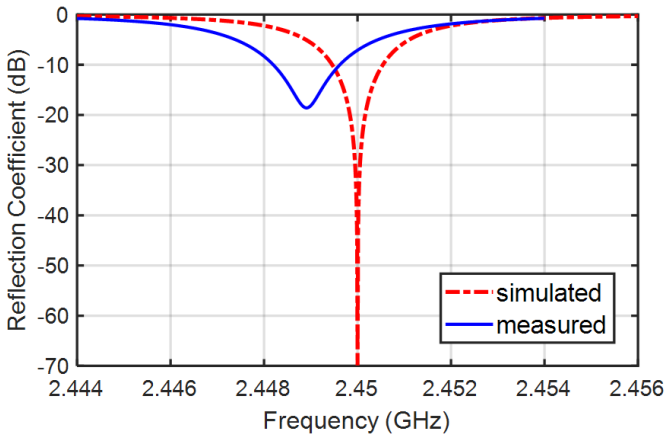


Fig. 6. Comparison of the EVA cavity plasma jet's simulated and measured reflection coefficients ($S_{11}$).

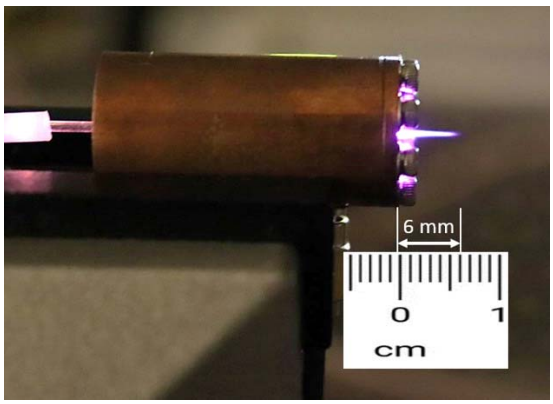


Fig. 7. Sample image of the fabricated EVA plasma jet in ON mode: a 6-mm long helium plasma jet under 5 W input power at 2.45 GHz and a gas flow rate of 7 slpm.

In this case, input power to the device port was 5 W at 2.45 GHz with a helium gas flow rate of 7 slpm. The plasma jet length was measured to be about 6 mm, while this length depends on the input power and, even more importantly, the gas flow rate. The generated plasma jet was touchable, and its temperature depends mainly on the value of microwave input power. In Fig. 7, light is also observed at the bottom of the structure where the gas flow comes in. Since the gas flow provided by a MFC is toward the jet direction with no mismatch in the gas flow path, this is likely the light reflection, through the glass capillary tube, of the plasma ignited inside the critical gap area.

The first step in generating a stable plasma is to make the gas break down. The breakdown voltage lies between the dark and glow discharge regimes. For discharge ignition, reaching the breakdown voltage (field) level in pre-breakdown is necessary. After the plasma is formed (post breakdown), it can typically be sustained at lower power than is needed for breakdown. Fig. 8 presents the measured breakdown power and $E$-field as a function of the gas flow rate in the capillary tube. It must be noted that the breakdown fields were extracted from HFSS simulations by incorporating the measured breakdown powers from the experiment. The breakdown power/voltage increases with a higher gas flow

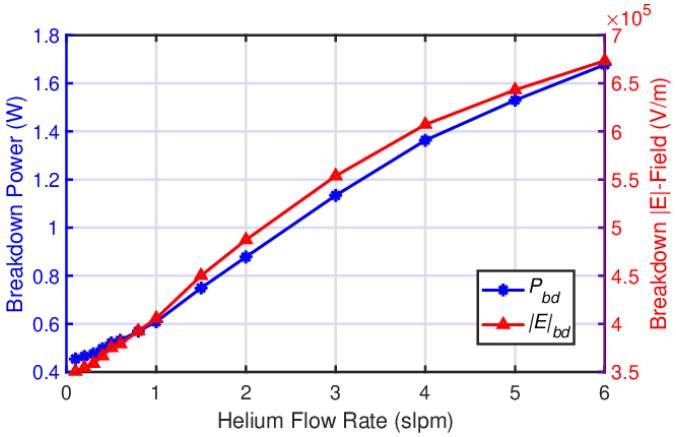


Fig. 8. Measured breakdown power and extracted $E$-field of the device under test at different helium flow rates up to 6 slpm.

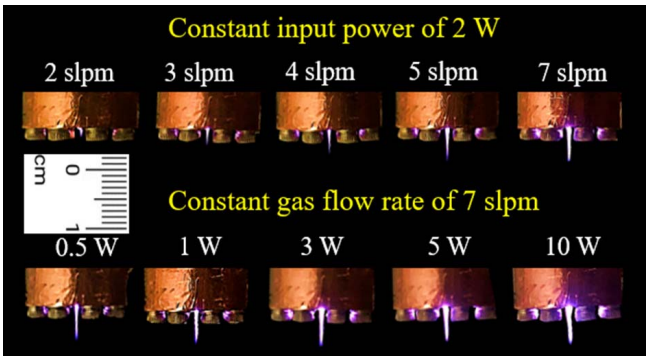


Fig. 9. Images of EVA cavity-based 2.45 GHz helium plasma jets at different gas flow rates and input powers.

rate. This is consistent with the literature [24], [25], and could be due to the electron production-loss rate. Higher collision frequencies increase the electron loss rate at higher gas flow rates. However, the electron production rate remains almost the same, which results in a higher electric field (or power) to ignite the plasma jet at a higher flow rate. Therefore, it is easier to first ignite the plasma jet at a lower flow rate and then increase the gas flow if a longer or higher density jet is required. It is also seen that for the helium flow rate in the range of 0.1–6 slpm, the breakdown power varies from about 450 mW–1.65 W, proving the low-power performance of the introduced microwave plasma jet. The correspondent breakdown $E$-field is in the order of $10^5$ V/m across the same range of gas flow rate. As mentioned earlier, the plasma sustaining power in post-breakdown is always less than the breakdown power. In this case, it was possible to sustain the plasma jet even with as low as 400 mW of input power at 2.45 GHz for the entire range of 0.1–6 slpm of helium flow rate, although the jet length and intensity strongly depend on that flow rate.

To investigate the effect of the gas flow rate on the plasma jet, the input power was set at a constant value of 2 W at the resonant frequency of 2.45 GHz, and the gas flow rate was varied from 2 to 7 slpm. As observed in the top row of Fig. 9, with the gas flow rate increase, the jet's length keeps increasing. It is noted that because of the specific model of the MFC in the measurement setup, it was not possible to test the plasma jet length for flow rates of more than 7 slpm. Similarly and to study the effect of input microwave power, the gas flow rate was set at a constant value of 7 slpm and the input power was varied from 0.5 to 10 W. As displayed in the bottom row of Fig. 9, although increasing the input power slightly enhanced the jet length, the noticeable effect was the increase in the plasma intensity by the input power.

Although the designed EVA cavity plasma jet has an excellent OFF-mode reflection performance, as depicted in Fig. 6, after plasma formation in the critical gap area of the EVA resonator, its frequency response varies significantly. Assuming negligible loss, the plasma absorbed power can be calculated as the difference between the input and reflected powers. Using a bidirectional coupler and two power sensors, as shown in Fig. 5, it is possible to accurately measure the input and reflected powers at the device's port. Fig. 10(a) displays the absorbed power for different input powers and gas flow rates. It is seen that the plasma absorbs more power at higher gas flow rates. Plasma power efficiency is the ratio of the absorbed power to the input power available to the EVA cavity jet, plotted in Fig. 10(b). It is noted that power efficiency significantly increases in lower input power values and is also enhanced considerably by gas flow rates. With 0.5 W of input power at a helium gas flow rate of 7 slpm, about 80% of the input microwave power is absorbed by the plasma, showing a high-efficiency plasma jet generation. The decrease in power efficiency by increasing input power is due to the reduction of the resonator quality factor. By plasma ignition in the critical gap area, the resonator gap capacitor ($C_{\text{gap}}$) becomes lossy because of plasma conductivity. The higher the input power, the higher plasma electron density, which eventuates higher loss and lower quality factor.

## IV. Diagnostics of the EVA Plasma Jet

Various optical diagnostics techniques are performed on APPJs based on the parameters to be measured. Electron density is one of the crucial parameters for different applications. Thomson scattering [26], [27] is an active spectroscopy method, allowing simultaneous electron density and temperature determination with high spectral resolution. While this method is widely used in high-density plasma characterization, it is expensive for low-density plasmas since a triple grating monochromator must be used to subtract the Rayleigh scattering component and stray light. Optical Emission Spectrometry (OES) [28], [29] is a passive spectroscopy method in which electron density is obtained by analyzing spectral line shapes and intensities. Two of the most commonly used broadening profiles to assess $n_e$ are spectral line emissions of the hydrogen atom, namely Balmer-alpha ($H$-$\alpha$) at 656.279 nm and Balmer-beta ($H$-$\beta$) at 486.135 nm, because of their position in the visible spectral region and linear Stark effect.

In atmospheric pressure plasmas, a spectral profile is a convolution of Gaussian and Lorentzian profiles, known as the Voigt function. The Gaussian component of the obtained spectral profile depends on the mass of the hydrogen atoms, central wavelength, and gas temperature. The Lorentzian component of the Voigt profile, that dominates the spectral profile, consists of Doppler, Resonance, van der Waals, and Stark broadenings [30]. The Resonance broadening occurs when

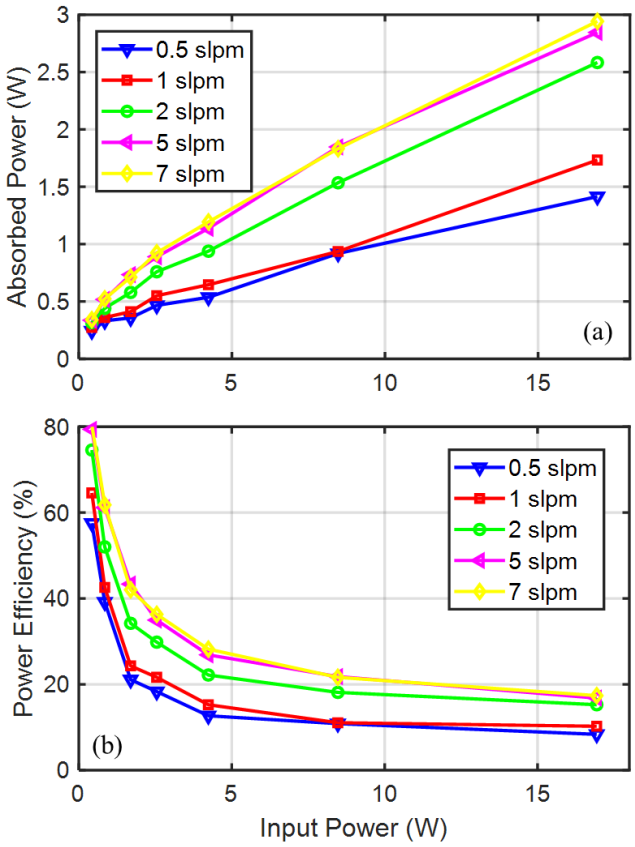


Fig. 10. Measured (a) plasma absorbed power and (b) power efficiency of the EVA cavity plasma jet for different input powers and helium flow rates.

perturbations of atomic levels are caused due to interaction between pairs of neutral atoms of the same kind, for example, (He + He). This broadening is negligible for hydrogen Balmer lines at atmospheric pressure and can be excluded [30]. Thus, Doppler and van der Waals broadenings must be considered for proper electron density estimation. When the emitting atoms have random motion, it introduces the Doppler effect, resulting in the broadening of atomic transitions, known as Doppler broadening. The full width at half maximum (FWHM) for Doppler broadening can be given as [30]

$$\Delta\lambda_D = \lambda_0\left(8\ln 2\frac{k_B T_g}{m_a c^2}\right) \tag{6}$$

where the gas temperature $T_g$ is in Kelvin, Boltzmann's constant $k_B$ is in $JK^{-1}$, and $m_a$ is the mass of the emitter. On the other hand, van der Waals broadening occurs when perturbations of atomic levels are caused due to interaction between different species, for example, (H + He). The FWHM of van der Waals broadening can be represented as [31]

$$\Delta\lambda_{\text{vdw}} = \frac{C}{{T_g}^{0.7}} \tag{7}$$

where the constant $C$ depends on the gas type and is equal to 2.42 and 5.12 for helium and argon, respectively.

To estimate van der Waals and Doppler broadening, the knowledge of gas temperature is essential. In nonthermal plasmas, the rotational temperature of diatomic molecules, mostly OH and $N_2^+$, give a close approximation of gas temperature, and this is a widely used method with great success [32]. The spectral profiles are measured utilizing an OES technique using a Teledyne Princeton Instruments HRS-500-SS spectrometer with 0.05 nm optical resolution. Fig. 11 exhibits the plasma jet generation and diagnostics setup. As the zoomed-in view shows, the optical fiber is placed closely toward the plasma jet to collect as much light as possible to get a distinctive spectral line for different operating conditions. This article uses transition lines of both OH (308–312 nm) [33] and $N_2^+$ (426–428.5 nm) [34] for cross-referencing the values. The experimental profiles are then compared with spectral profiles available in LIFBASE software, as displayed in Fig. 12(a) and (b), LIFBASE is a software that contains the spectral database of diatomic molecules. As both $N_2^+$ and OH spectra were measured through OES, the rotational temperatures for all input powers were extracted by comparing the measured spectrum with the LIFBASE generated spectrum for that particular diatomic molecule.

TABLE II
MEASURED GAS TEMPERATURES AND EXTRACTED VARIOUS SPECTRUM BROADENINGS OF THE 2.45 GHz EVA PLASMA JET AT VARIOUS INPUT POWERS AND HELIUM FLOW RATE OF 7 slpm

| Input Power | 0.5 W | 1 W | 5 W | 10 W |
|---|---|---|---|---|
| $T_g$ (K) | 296 | 333 | 340 | 350 |
| $\Delta\lambda_{Stark}$ (nm) | 0.1952 | 0.198 | 0.1946 | 0.1946 |
| $\Delta\lambda_D$ (nm) | 0.0087 | 0.0067 | 0.006 | 0.0068 |
| $\Delta\lambda_{vdw}$ (nm) | 0.0451 | 0.0415 | 0.0409 | 0.0401 |

As seen in Table II, the gas temperature increases from 296 (ambient) to 350 K for the change of input power from 500 mW to 10 W. All measured temperatures are with the accuracy of ±5 K. This temperature range proves this device as a safe option for many applications sensitive to high temperature. Upon measuring $T_g$, the Doppler and van der Waals broadenings are calculated using (6) and (7), respectively. Comparing the values in Table II, it is evident that the van der Waals and the Doppler broadenings are minimal and the Stark broadening is mostly dominant, making its FWHM suitable to measure $n_e$. Hence, this article presents measurements of the electron density in the introduced EVA plasma jet using the OES Stark broadening technique. In this study, the $H$-$\alpha$ profile was opted for calculating $n_e$ as it is more distinct than the $H$-$\beta$ for the EVA jet device. Fig. 13 displays a sample normalized $H$-$\alpha$ profile recorded at 1 W input power and 7 slpm of helium flow rate. Such a profile is then used to extract FWHM of spectral broadening, represented by $\Delta\lambda_{\text{Stark}}$ in nm, which is directly related to $n_e$ by

$$n_e = 10^{17} \times (\Delta\lambda_{\text{Stark}}/1.098)^{1.47135} \tag{8}$$

where $n_e$ is in $cm^{-3}$ [35].

To investigate the effect of input 2.45 GHz power on the EVA jet electron density, the gas flow rate was kept constant at 7 slpm, and $n_e$ was measured at input powers ranging from 0.5 to 10 W, as seen in Fig. 14. It is observed that electron density is in the range of $8 \times 10^{15}$ $cm^{-3}$, which is significant considering the input power range. Higher electron density over the lower range of input power is practically significant

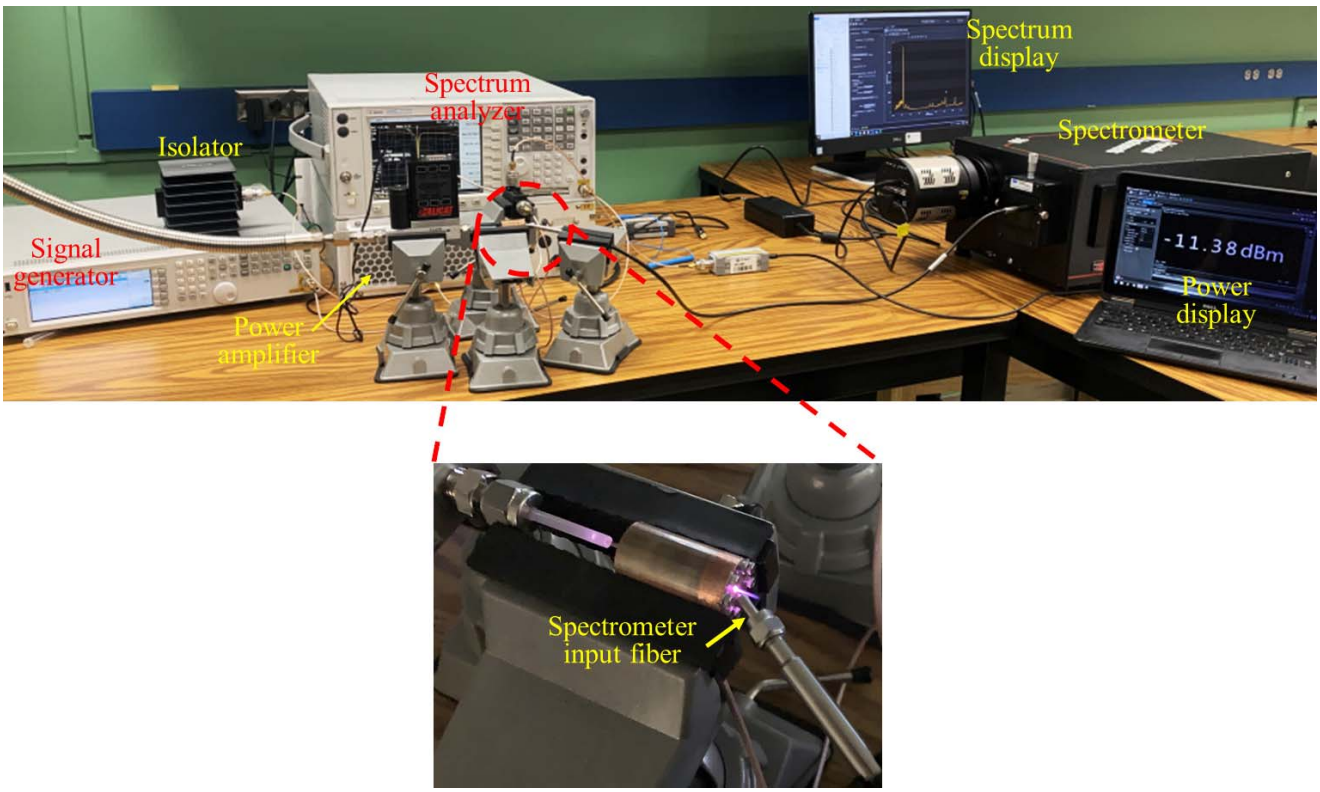


Fig. 11. EVA microwave plasma jet measurement and diagnostics set up with the main device zoomed in. A 2.45 GHz signal is generated by a signal generator and amplified by a power amplifier, gas flow to the EVA cavity resonator is provided through a capillary tube, and the jet's light is fed into the spectrometer by a fiber optic probe.

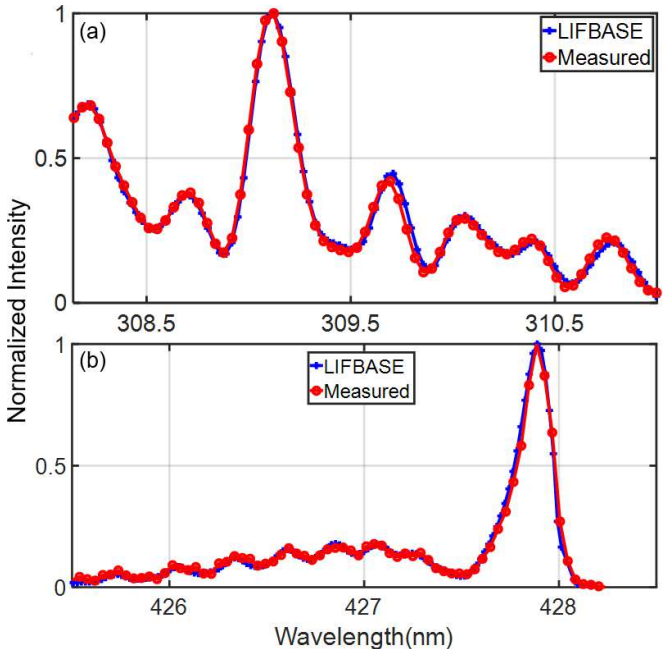


Fig. 12. Normalized (a) OH spectrum fit at 309 nm for input power of 10 W with extracted $T_g = 350$ K, (b) $N_2^+$ spectrum fit at 428 nm for input power of 500 mW with extracted $T_g = 296$ K.

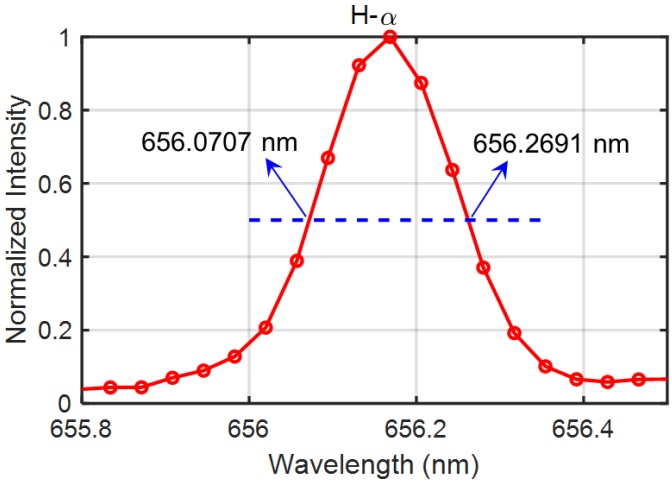


Fig. 13. Normalized $H$-$\alpha$ line at 1 W of 2.45 GHz input power and 7 slpm helium flow rate. FWHM is indicated for reading the $\Delta\lambda_s^A$, which is required to extract the jet electron density.

and is due to the higher efficiency of this device at lower input powers, as depicted in Fig. 10(b). Variation of electron density by gas flow rate (ranging from 3 to 7 slpm) for different input power values (0.5, 1, and 3 W) is represented in Fig. 15. Again, it is observed that the electron density of the EVA plasma jet remains almost constant around $8 \times 10^{15}$ cm$^{-3}$. This is because the jet absorbed power increases slightly by input power and gas flow rate as the power efficiency decreases, as depicted in Fig. 10. Practically, it is a big advantage to have such a strong plasma jet even with 100 s of milliwatts input power and flow rate of just a few slpm, as it makes the device very safe for a variety of applications.

TABLE III
COMPARISON OF THE INTRODUCED EVA CAVITY PLASMA JET WITH OTHER STATE-OF-THE-ART 2.45 GHz RESONANT PLASMA JETS

| | Input Power (W) | Electron Density ($cm^{-3}$) | Jet Length (mm) | Resonator Type | Gas Flow Rate | Efficiency (%) |
|---|---|---|---|---|---|---|
| [18] | 40 | N/M | 3 | CTL-APPJ | 2 l/min | 89.6 |
| [36] | 0.5 | $4\times10^{14}$ | 7 | coaxial | 2 slpm, Ar | 50-85 |
| [37] | 850 | $4.46\times10^{16}$ | 20 | cavity | 7-35 lpm, He | N/M |
| [38] | 2-10 | $10^{15}$ | 10 | coaxial | 2 slpm | 46.5 (at 8.1 W) |
| [39] | 88 | $10^{15}$ | 5 | CTLR | 0.68 slm He+15.5 sccm $N_2$ | N/M |
| [40] | 40 | $10^{13}$ | N/M | coaxial $\lambda/4$ | N/M, Ar+N | 80 |
| This work | $> 0.5$ | $> 7.6\times10^{15}$ | 6 (max) | EVA cavity | 1-7 slpm, He | $> 80$ (max) |

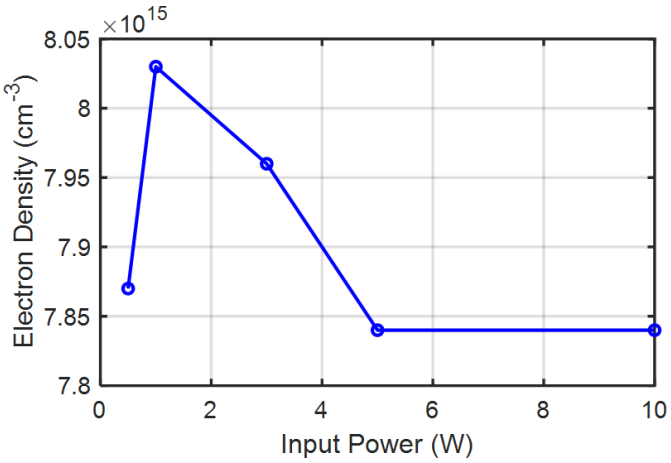


Fig. 14. Measured electron number density at a helium flow rate of 7 slpm and different values of 2.45 GHz input powers.

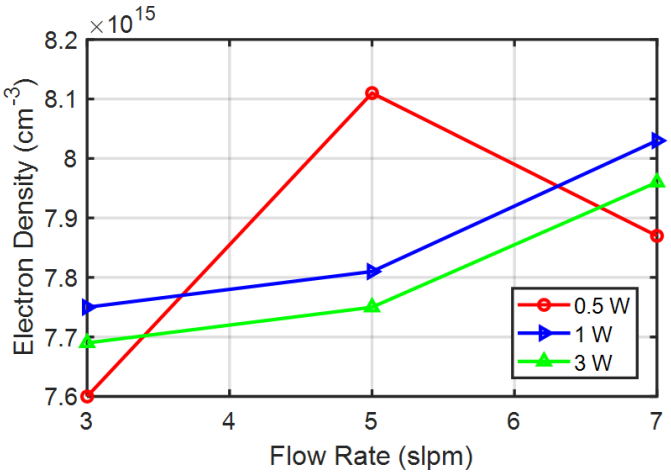


Fig. 15. Extracted electron density at three flow rates of 3, 5, and 7 slpm and three 2.45 GHz input powers of 0.5, 1, and 3 W.

Table III compares the EVA cavity plasma jet introduced in this article with other state-of-the-art 2.45 GHz resonant microwave plasma jets found in the literature. It is seen that overall, this new device provides the best performance. Notably, it has higher electron density compared with similar low-power-consumption jets and higher efficiency compared with higher power devices.

## V. CONCLUSION

A new resonant microwave plasma jet technology has been demonstrated in this work. The structure is formed by an EVA cavity resonator with a helium flow going through its critical gap region. Since this is a high-$Q$ resonant structure with an electric field mainly concentrated over that critical gap area, gas breakdown occurs even with low values of input microwave power. The gas flow then pushes the plasma torch out of the resonator in a jet form, where its properties depend on both input power and gas flow rate. A prototype 2.45 GHz EVA plasma jet provided a maximum efficiency of $>80\%$, achieved under low power and high flow rate, with electron density in the range of $10^{15}$ ($cm^{-3}$) and a maximum jet temperature of 350 K at 10 W input power. The results prove the possibility of realizing high-density plasma jets with only milliwatts of power by employing high-$Q$ microwave resonant structures. If required, the plasma volume can be extended by either using an array of such jets or scaling the resonator to lower frequencies.

## REFERENCES

[1] G. Fridman, G. Friedman, A. Gutsol, A. B. Shekhter, V. N. Vasilets, and A. Fridman, "Applied plasma medicine," *Plasma Process. Polym.*, vol. 5, no. 6, pp. 503–533, Aug. 2008.
[2] B. P. Dirks, D. Dobrynin, G. Fridman, Y. Mukhin, A. Fridman, and J. J. Quinlan, "Treatment of raw poultry with nonthermal dielectric barrier discharge plasma to reduce *Campylobacter jejuni and Salmonellaenterica*," *J. Food Protection*, vol. 75, no. 1, pp. 22–28, Jan. 2012.
[3] N. Bahrami, D. Bayliss, G. Chope, S. Penson, T. Perehinec, and I. D. Fisk, "Cold plasma: A new technology to modify wheat flour functionality," *Food Chem.*, vol. 202, pp. 247–253, Jul. 2016.
[4] Y. P. Raizer, M. N. Shneider, and N. A. Yatsenko, *Radio-Frequency Capacitive Discharges*, Boca Raton, FL, USA: CRC Press, 1995.
[5] M. A. Lieberman and A. J. Lichtenberg, *Principle of Plasma Discharge and Materials Processing*. New York, NY, USA: Wiley, 2005.
[6] A. Semnani, S. O. Macheret, and D. Peroulis, "A high-power widely tunable limiter utilizing an evanescent-mode cavity resonator loaded with a gas discharge tube," *IEEE Trans. Plasma Sci.*, vol. 44, no. 12, pp. 3271–3280, Dec. 2016.
[7] A. Semnani, D. Peroulis, and S. O. Macheret, "Plasma-enabled tuning of a resonant RF circuit," *IEEE Trans. Plasma Sci.*, vol. 44, no. 8, pp. 1396–1404, Aug. 2016.
[8] L. Bárdos and H. Baránková, "Cold atmospheric plasma: Sources, processes, and applications," *Thin Solid Films*, vol. 518, no. 23, pp. 6705–6713, Sep. 2010.
[9] F. Iza and J. A. Hopwood, "Low-power microwave plasma source based on a microstrip split-ring resonator," *IEEE Trans. Plasma Sci.*, vol. 31, no. 4, pp. 782–787, Aug. 2003.

[10] B.-D. Huang, X.-M. Zhu, W.-C. Chen, and Y.-K. Pu, "The evolution of the optical emission pattern from a pulsed microwave-excited microstrip split-ring resonator microplasma," *IEEE Trans. Plasma Sci.*, vol. 42, no. 10, pp. 2772–2773, Oct. 2014.
[11] Z. Chen *et al.*, "Characteristic plume morphologies of atmospheric Ar and He plasma jets excited by a pulsed microwave hairpin resonator," *Chin. Phys. B*, vol. 27, no. 5, May 2018, Art. no. 055202.
[12] S. T. Lee, W. J. Nam, J. K. Lee, and G. S. Yun, "*In situ* impedance measurement of microwave atmospheric pressure plasma," *Plasma Sources Sci. Technol.*, vol. 26, no. 4, Mar. 2017, Art. no. 045004.
[13] J. Hopwood, A. R. Hoskinson, and J. Gregório, "Microplasmas ignited and sustained by microwaves," *Plasma Sources Sci. Technol.*, vol. 23, no. 6, Dec. 2014, Art. no. 064002.
[14] S. Dennison, A. Chapman, W. Luo, M. Lanagan, and J. Hopwood, "*In situ* impedance measurement of microwave atmospheric pressure plasma," *Plasma Sources Sci. Technol.*, vol. 25, no. 3, Mar. 2016, Art. no. 03LT02.
[15] N. Srivastava and C. Wang, "Determination of OH radicals in an atmospheric pressure helium microwave plasma jet," *IEEE Trans. Plasma Sci.*, vol. 39, no. 3, pp. 918–924, Mar. 2011.
[16] J. Kim, H. Sakakita, H. Ohsaki, and M. Katsurai, "Microwave-excited atmospheric pressure plasma jet with wide aperture for the synthesis of carbon nanomaterials," *Jpn. J. Appl. Phys.*, vol. 54, no. 1S, Jan. 2015, Art. no. 01AA02.
[17] S. K. Kwon, S.-J. Park, I. H. Won, C. Ahn, and J.-Y. Sim, "Microwave plasma generation with resonance frequency tracking and power regulation," *IEEE Trans. Plasma Sci.*, vol. 45, no. 6, pp. 925–931, Jun. 2017.
[18] W. Fu, C. Zhang, C. Nie, X. Li, and Y. Yan, "A high efficiency low-temperature microwave-driven atmospheric pressure plasma jet," *Appl. Phys. Lett.*, vol. 114, no. 25, Jun. 2019, Art. no. 254106.
[19] A. Semnani, S. O. Macheret, and D. Peroulis, "A quasi-absorptive microwave resonant plasma switch for high-power applications," *IEEE Trans. Microw. Theory Techn.*, vol. 66, no. 8, pp. 3798–3806, Aug. 2018.
[20] M. S. Arif and D. Peroulis, "A 6 to 24 GHz continuously tunable, microfabricated, high-Q cavity resonator with electrostatic MEMS actuation," in *IEEE MTT-S Int. Microw. Symp. Dig.*, Jun. 2012, pp. 1–3.
[21] H. Joshi, H. H. Sigmarsson, D. Peroulis, and W. J. Chappell, "Highly loaded evanescent cavities for widely tunable high-Q filters," in *IEEE MTT-S Int. Microw. Symp. Dig.*, Jun. 2007, pp. 2133–2136.
[22] Y.-M. Lee, J.-K. Kim, and J. Hur, "Study on the empirical design of open-ended coaxial cavity resonator," *Microw. Opt. Technol. Lett.*, vol. 56, no. 3, pp. 606–610, Mar. 2014.
[23] A. Anand, J. Small, D. Peroulis, and X. Liu, "Theory and design of octave tunable filters with lumped tuning elements," *IEEE Trans. Microw. Theory Techn.*, vol. 61, no. 12, pp. 4353–4364, Dec. 2013.
[24] Z. Ouyang, V. Surla, T. S. Cho, and D. N. Ruzic, "Characterization of an atmospheric-pressure helium plasma generated by 2.45-GHz microwave power," *IEEE Trans. Plasma Sci.*, vol. 40, no. 12, pp. 3476–3481, Dec. 2012.
[25] L. M. D. Rosario *et al.*, "Characterization of a microwave-induced atmospheric-pressure Ar–$N_2$ plasma pencil," *IEEE Trans. Plasma Sci.*, vol. 45, no. 2, pp. 301–309, Feb. 2017.
[26] H. J. Van Der Meiden *et al.*, "High sensitivity imaging Thomson scattering for low temperature plasma," *Rev. Sci. Instrum.*, vol. 79, no. 1, Jan. 2008, Art. no. 013505.
[27] B. L. M. Klarenaar, O. Guaitella, R. Engeln, and A. Sobota, "How dielectric, metallic and liquid targets influence the evolution of electron properties in a pulsed he jet measured by Thomson and Raman scattering," *Plasma Sources Sci. Technol.*, vol. 27, no. 8, Aug. 2018, Art. no. 085004.
[28] J. Ashkenazy, R. Kipper, and M. Caner, "Spectroscopic measurements of electron density of capillary plasma based on Stark broadening of hydrogen lines," *Phys. Rev. A, Gen. Phys.*, vol. 43, no. 10, pp. 5568–5574, May 1991.
[29] N. Konjević, A. Lesage, J. R. Fuhr, and W. L. Wiese, "Experimental stark widths and shifts for spectral lines of neutral and ionized atoms (A critical review of selected data for the period 1989 through 2000)," *J. Phys. Chem. Reference Data*, vol. 31, no. 3, pp. 819–927, Sep. 2002.
[30] A. Yu Nikiforov, C. Leys, M. A. Gonzalez, and J. L. Walsh, "Electron density measurement in atmospheric pressure plasma jets: Stark broadening of hydrogenated and non-hydrogenated lines," *Plasma Sources Sci. Technol.*, vol. 24, no. 3, Apr. 2015, Art. no. 034001.
[31] H. Wang, R. J. Wandell, K. Tachibana, J. Voráč, and B. R. Locke, "The influence of liquid conductivity on electrical breakdown and hydrogen peroxide production in a nanosecond pulsed plasma discharge generated in a water-film plasma reactor," *J. Phys. D: Appl. Phys.*, vol. 52, no. 7, Feb. 2019, Art. no. 075201.
[32] P. J. Bruggeman, N. Sadeghi, D. C. Schram, and V. Linss, "Gas temperature determination from rotational lines in non-equilibrium plasmas: A review," *Plasma Sources Sci. Technol.*, vol. 23, Apr. 2014, Art. no. 023001.
[33] Z.-S. Chang, G.-J. Zhang, X.-J. Shao, and Z.-H. Zhang, "Diagnosis of gas temperature, electron temperature, and electron density in helium atmospheric pressure plasma jet," *Phys. Plasmas*, vol. 19, no. 7, Jul. 2012, Art. no. 073513.
[34] M. C. García, C. Yubero, M. D. Calzada, and M. P. Martínez-Jiménez, "Spectroscopic characterization of two different microwave (2.45 GHz) induced argon plasmas at atmospheric pressure," *Appl. Spectrosc.*, vol. 59, no. 4, pp. 519–528, Apr. 2005.
[35] M. A. Gigosos, M. A. Gonzalez, and V. Cardenoso, "Computer simulated Balmer-alpha, -beta and -gamma Stark line profiles for non-equilibrium plasmas diagnostics," *Spectrochim. Acta B, At. Spectrosc.*, vol. 58, no. 6, pp. 1489–1504, Aug. 2003.
[36] J. Choi, F. Iza, H. J. Do, J. K. Lee, and M. H. Cho, "Microwave-excited atmospheric-pressure microplasmas based on a coaxial transmission line resonator," *Plasma Sources Sci. Technol.*, vol. 18, no. 2, May 2009, Art. no. 025029.
[37] A. Gulec, F. Bozduman, and A. M. Hala, "Atmospheric pressure 2.45-GHz microwave helium plasma," *IEEE Trans. Plasma Sci.*, vol. 43, no. 3, pp. 786–790, Mar. 2015.
[38] S. T. Lee, W. J. Nam, J. K. Lee, and G. S. Yun, "*In situ* impedance measurement of microwave atmospheric pressure plasma," *Plasma Sources Sci. Technol.*, vol. 26, no. 4, Mar. 2017, Art. no. 045004.
[39] N. Srivastava and C. Wang, "Effect of $N_2$ and $O_2$ on OH radical production in an atmospheric helium microwave plasma jet," *Plasma Sci. Technol.*, vol. 21, no. 11, Nov. 2019, Art. no. 115401.
[40] H.-E. Porteanu, D. Wolf, and W. Heinrich, "Frequency dependence of the capacitive excitation of plasma: An experimental proof," *J. Appl. Phys.*, vol. 127, no. 18, May 2020, Art. no. 183301.

**Abbas Semnani** (Senior Member, IEEE) received the B.Sc. degree from the University of Tehran (UT), Tehran, Iran, in 2000, and the M.Sc. and Ph.D. degrees from the K. N. Toosi University of Technology, Tehran, in 2002 and 2009, respectively, all in electrical engineering.

He is currently an Assistant Professor with the Department of Electrical Engineering and Computer Science, The University of Toledo, Toledo, OH, USA. Before joining the UT in 2019, he has been with Purdue University, West Lafayette, IN, USA, since 2012, where he focused on plasma-electromagnetic (EM) interactions and plasma for high-power radio frequency (RF) tuning. Prior to that, he served as a Research and Teaching Associate with the Department of Electrical and Computer Engineering, K. N. Toosi University of Technology, from 2009 to 2012. During his Ph.D., he was a Visiting Scholar at Aristotle University of Thessaloniki, Thessaloniki, Greece, in 2008, where he focused on novel computational techniques for solving time-domain inverse scattering problems. His current research interests include high-power microwaves, low-temperature plasmas, reconfigurable RF electronics, tunable antennas, and RF nanotechnology.

Dr. Semnani has received the 2019 IEEE MTT-S "Tatsuo Itoh" Award and NASA Faculty Fellowship in 2022.

**Kazi Sadman Kabir** was born in Jashore, Bangladesh, in 1993. He received the bachelor's degree in electrical and electronics engineering from the Ahsanullah University of Science and Technology, Dhaka, Bangladesh, in 2016, and the M.Sc. degree in electrical engineering from the South Dakota School of Mines and Technology, Rapid City, SD, USA, in 2020. He is currently pursuing the Ph.D. degree with the Department of Electrical Engineering and Computer Science, The University of Toledo, Toledo, OH, USA.

His research interests include plasma jets, electromagnetics (EMs), radio frequency (RF) circuits, and 3-D-printed antennas.